Atmospheric
Chemistry
and Physics

Supplement of

An assessment of land energy balance over East Asia from multiple lines of evidence and the roles of the Tibet Plateau, aerosols, and clouds

Qiuyan Wang et al.

Correspondence to: Hua Zhang (huazhang@cma.gov.cn)

Supplemental Figures and Tables.
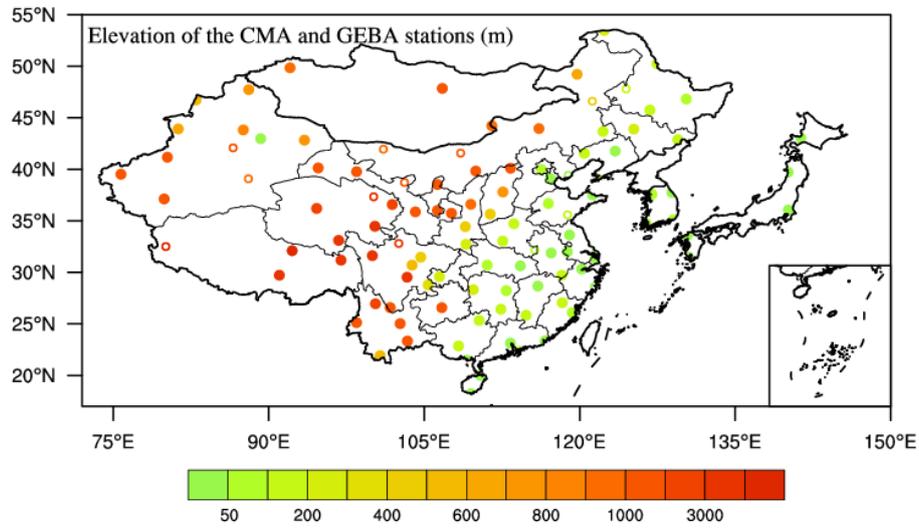
Figure S1. Geographical distribution and elevation (Units: m) of all observational sites from the CMA (99 sites) and GEBA (16 sites). The solid and hollow circles indicate rural (19 vs. 18 for all-sky and clear-sky conditions) and urban stations (96 vs. 74), respectively.

Table S1. CMA (99 stations) and GEBA (16 stations) observational sites sorted by station numbers, as well as their latitudes (positive north/negative south), longitudes (positive east/negative west), altitudes (m), station name, country/regions, data sources, and administrative level.

Station NO.	lat	lon	Altitude	Station name, Country/region, data sources	Administrative level
863	22.32	114.17	66	Hong Kong (WRDC), China	city
880	43.05	141.33	17	Sapporo (WRDC+BSRN), Japan	city
881	39.72	140.1	9	Akita (WRDC), Japan	city
886	36.05	140.13	25	Tateno (WRDC+BSRN), Japan	city
889	33.58	130.38	3	Fukuoka (WRDC+BSRN), Japan	city
892	31.57	130.55	4	Kagoshima (WRDC), Japan	island
893	27.08	142.18	4	Chichijima (WRDC), Japan	island
894	26.23	127.68	35	Naha (WRDC), Japan	city
895	24.33	124.17	6	Ishigakijima (WRDC+BSRN), Japan	island
896	24.3	153.97	8	Minamitorishima (WRDC+BSRN), Japan	island
901	37.75	128.9	26	Kangnung (WRDC), Korea (South)	city
902	37.57	126.97	86	Seoul (WRDC), Korea (South)	city
903	35.1	129.03	69	Pusan (WRDC), Korea (South)	city
904	34.78	126.38	53	Mokpo (WRDC), Korea (South)	city
906	49.85	92.07	934	Ulaangom (WRDC), Mongolia	city
908	47.85	106.75	1264	Ulan-Bator (WRDC), Mongolia	city
50136	53.47	122.37	296	Mohe, Heilongjiang (CMA)	city-governed district
50468	50.25	127.45	165.8	Heihe, Heilongjiang (CMA)	city-governed district
50527	49.22	119.75	612.9	Hailaer, Inner Mongolia (CMA)	city-governed district
50742	47.8	124.48	162.4	Fuyu, Heilongjiang (CMA)	county
50834	46.6	121.22	499.7	Suolun, Inner Mongolia (CMA)	town
50873	46.82	130.28	81.2	Jiamusi, Heilongjiang (CMA)	city

50953	45.75	126.77	146	Haerbin, Heilongjiang (CMA)	city
51076	47.73	88.08	735.1	Altay, Xinjiang (CMA)	county-level city
51133	46.73	83	534.9	Tacheng, Xinjiang (CMA)	city
51431	43.92	81.28	664	Yining, Xinjiang (CMA)	county-level city
51463	43.82	87.55	850.5	Urumqi, Xinjiang (CMA)	city
51567	42.08	86.57	1055.3	Yanqi, Xinjiang (CMA)	county
51573	42.97	89.23	34.5	Turpan , Xinjiang (CMA)	city
51628	41.17	80.23	1103.8	Aksu , Xinjiang (CMA)	city-governed district
51709	39.52	75.75	1289	Kashgar, Xinjiang (CMA)	city
51777	39.08	88.05	950	Ruoqiang, Xinjiang (CMA)	county
51828	37.12	79.92	1387	hotan, Xinjiang (CMA)	county-level city
52203	42.83	93.45	737.9	Hami, Xinjiang (CMA)	county-level city
52267	41.95	101.07	940.5	Ejin Banner, Inner Mongolia (CMA)	Banner, smaller than county
52418	40.13	94.78	1138.2	Dunhuang, Gansu (CMA)	county-level city
52533	39.77	98.48	1477.2	Jiuquan, Gansu (CMA)	city
52681	38.72	103.1	1353.7	Minqin, Gansu (CMA)	county
52754	37.33	100.13	3301.5	Gangca, Qinghai (CMA)	county
52818	36.2	94.63	2806.1	Golmud, Qinghai (CMA)	sub-prefecture-level city
52866	36.58	101.92	2244.2	Xining, Qinghai (CMA)	city
52983	35.87	104.15	1874.4	Lanzhou (Yuzhong), Gansu (CMA)	city
53068	44.22	111.53	964.8	Erenhot, Inner Mongolia (CMA)	city
53336	41.57	108.52	1288	Hailiut, Inner Mongolia (CMA)	town
53487	40.1	113.33	1067.6	Datong, Shanxi (CMA)	city
53543	39.83	109.98	1460.4	Dongsheng, Inner Mongolia (CMA)	city-governed district
53614	38.52	106.27	1111.5	Yinchuan, Ningxia (CMA)	city
53772	37.8	112.6	783.7	Taiyuan, Shanxi (CMA)	city
53817	36	106.27	1752.2	Guyuan, Ningxia (CMA)	city
53845	36.6	109.5	957.8	Yanan, Shannxi (CMA)	city
53923	35.73	107.63	1421	Xifeng, Shannxi (CMA)	city-governed district
53963	35.65	111.37	434.4	Houma, Shanxi (CMA)	county-level city
54102	43.95	116.07	989.5	Xilinhot , Inner Mongolia (CMA)	city
54135	43.67	122.25	179.5	Tongliao, Inner Mongolia (CMA)	city
54161	43.9	125.22	236.8	Changchun, Jilin (CMA)	city
54292	42.88	129.47	176.8	Yanji, Jilin (CMA)	county-level city
54324	41.55	120.45	168.7	Chaoyang, Liaoning (CMA)	city
54342	41.77	123.43	41.6	Shenyang, Liaoning (CMA)	city
54511	39.97	116.32	50.6	Beijing (CMA)	city
54527	39.1	117.17	3.3	Tianjing (CMA)	city
54539	39.42	118.9	10.5	Laoting, Hebei (CMA)	county
54662	39.02	121.72	62.4	Dalian, Liaoning (CMA)	city
54764	37.5	121.25	32.6	Fushan, Shandong (CMA)	city
54823	36.68	116.98	51.6	Jinan, Shandong (CMA)	city

54936	35.58	118.83	107.4	Ju, Shandong (CMA)	county
55228	32.5	80.08	4278	Geer, Tibet (CMA)	county
55299	32.1	92.27	4366.1	Naqu, Tibet (CMA)	city
55591	29.72	91.03	3658	Lhasa, Tibet (CMA)	city
56029	33.1	96.75	3702.6	Yushu, Qinghai (CMA)	city
56043	34.47	100.25	3719	Guoluo, Qinghai (CMA)	city
56137	31.18	96.98	3175.4	Changdu, Tibet (CMA)	city
56146	31.62	100	3393.5	Ganzi, Sichuan (CMA)	city
56173	32.8	102.55	3492.7	Hongyuan, Sichuan (CMA)	county
56187	30.7	103.83	539.3	Wenjiang, Sichuan (CMA)	city
56196	31.47	104.67	470.8	Mianyang, Sichuan (CMA)	city
56385	29.52	103.35	3137	Mount Emei, Sichuan (CMA)	county-level city
56651	26.95	100.3	2393.2	Lijiang, Yunan (CMA)	city
56666	26.58	101.72	1190.1	Panzhihua, Sichuan (CMA)	city
56739	25.12	98.48	1627.5	Tengchong, Yunnan (CMA)	county-level city
56778	25.02	102.68	1891.3	Kunming, Yunnan (CMA)	city
56959	21.92	100.75	533	Jinghong, Yunnan (CMA)	county-level city
56985	23.33	103.38	1300.7	Mengzi, Yunnan (CMA)	county-level city
57083	34.72	113.65	109	Zhengzhou, Henan (CMA)	city
57131	34.43	108.97	410	Jinghe, Shannxi (CMA)	city
57178	33.03	112.58	129.2	Nanyang, Henan (CMA)	city
57245	32.72	109.03	290.8	Ankang, Shannxi (CMA)	city
57461	30.7	111.08	69.7	Yichang, Hubei (CMA)	city
57494	30.63	114.28	23	Wuhan, Hubei (CMA)	city
57516	29.58	106.47	259.1	Shapingba, Chongqing (CMA)	city-governed district
57604	28.78	105.38	368.8	Naxi, Sichuan (CMA)	city-governed district
57649	28.32	109.73	206.6	Jishou, Hunan (CMA)	county-level city
57687	28.22	112.92	68	Changsha, Hunan (CMA)	city
57816	26.57	106.7	1071.2	Guiyang, Guizhou (CMA)	city
57874	26.42	112.4	116.6	Changning, Hunan (CMA)	county-level city
57957	25.33	110.3	166.7	Guilin, Guangxi (CMA)	city
57993	25.83	114.83	124.8	Ganzhou, Jiangxi (CMA)	city
58141	33.63	119.02	14.4	Huaian, Jiangsu (CMA)	city
58208	32.17	115.67	56.9	Gushi, Henan (CMA)	county
58238	32	118.8	8.9	Nanjing, Jiangsu (CMA)	city
58265	32.07	121.6	5.5	Lvsi, Jiangsu (CMA)	town
58321	31.88	117.25	23.6	Hefei, Anhui (CMA)	city
58362	31.4	121.48	3.5	Shanghai (CMA)	city-governed district
58457	30.32	120.2	7.2	Hangzhou, Zhejiang (CMA)	city
58531	29.72	118.28	142.7	Tunxi, Anhui (CMA)	city-governed district
58606	28.67	115.97	47	Nanchang, Jiangxi (CMA)	city
58665	28.62	121.42	1.3	Hongjia, Zhejiang (CMA)	street
58737	27.05	118.32	154.9	Jianou, Fujian (CMA)	county-level city
58847	26.08	119.28	88.4	Fuzhou, Fujian (CMA)	city

59287	23.13	113.32	11.3	Guangzhou, Guangdong (CMA)	city
59316	23.35	116.67	4.3	Shantou, Guangdong (CMA)	city
59431	22.85	108.32	122.3	Nanning, Guangxi (CMA)	city
59644	21.48	109.12	15.3	Beihai, Guangxi (CMA)	city
59758	20	110.42	14.1	Haikou, Hainan (CMA)	city
59948	18.23	109.52	5.5	Sanya, Hainan (CMA)	city
59981	16.83	112.33	4.7	Xisha, Hainan (CMA)	city-governed district

Table S2. A list of 40 CMIP6 models used in this study.

Model name	Modeling groups	Resolution
ACCESS-CM2	Australian Research Council Centre of Excellence for Climate System Science, Australia	$1.25° \times 1.875°$
ACCESS-ESM1-5	Australian Research Council Centre of Excellence for Climate System Science, Australia	$1.25° \times 1.875°$
AWI-CM-1-1-MR	Alfred Wegener Institute, Helmholtz Centre for Polarand Marine Research (AWI), Germany	$1° \times 1°$
AWI-ESM-1-1-LR	Alfred Wegener Institute, Helmholtz Centre for Polarand Marine Research (AWI), Germany	$1.875° \times 1.875°$
BCC-CSM2-MR	Beijing Climate Center, China Meteorological Administration, China	$1.125° \times 1.125°$
BCC-ESM1	Beijing Climate Center, China Meteorological Administration, China	$2.81° \times 2.81°$
CAMS-CSM1-0	Chinese Academy of Meteorological Sciences, China	$1.125° \times 1.125°$
CanESM5	Canadian Centre for Climate, Canada	$2.81° \times 2.81°$
CESM2	National Center for Atmospheric Research, USA	$0.9° \times 1.25°$
CESM2-FV2	National Center for Atmospheric Research, USA	$1.875° \times 2.5°$
CESM2-WACCM	National Center for Atmospheric Research, USA	$0.9° \times 1.25°$
CESM2-WACCM-FV2	National Center for Atmospheric Research, USA	$1.875° \times 2.5°$
CIESM	Tsinghua University, China	$1° \times 1°$
E3SM-1-0	Lawrence Livermore National Laboratory, USA	$1° \times 1°$
E3SM-1-1	Lawrence Livermore National Laboratory, USA	$1° \times 1°$
E3SM-1-1-ECA	Lawrence Livermore National Laboratory, USA	$1° \times 1°$
EC-Earth3	European EC-Earth consortium	$0.7° \times 0.7°$
EC-Earth3-Veg	European EC-Earth consortium	$0.7° \times 0.7°$
EC-Earth3-Veg-LR	European EC-Earth consortium	$1.125° \times 1.125°$
FGOALS-f3-L	Institute of Atmospheric Physics, Chinese Academy of Sciences, China	$1° \times 1.25°$
FGOALS-g3	Institute of Atmospheric Physics, Chinese Academy of Sciences, China	$1° \times 1.25°$
GFDL-CM4	Geophysical Fluid Dynamics Laboratory, USA	$1.25° \times 1°$
GFDL-ESM4	Geophysical Fluid Dynamics Laboratory, USA	$1.25° \times 1°$
GISS-E2-1-G	Goddard Institute for Space Studies, New York, USA	$2° \times 2.5°$
GISS-E2-1-G-CC	Goddard Institute for Space Studies, New York, USA	$2° \times 2.5°$
GISS-E2-1-H	Goddard Institute for Space Studies, New York, USA	$2° \times 2.5°$

INM-CM4-8	Institute for Numerical Mathematics, Russia	1.5° × 2°
INM-CM5-0	Institute for Numerical Mathematics, Russia	1.5° × 2°
IPSL-CM6A-LR	Institute Pierre-Simon Laplace, France	2.5° × 1.27°
KACE-1-0-G	National Institute of Meteorological Sciences/Korea Meteorological Administration, Climate Research Division, Republic of Korea	1.25° × 1.85°
MIROC6	Japan Agency for Marine-Earth Science and Technology, Japan	1.4° × 1.4°
MPI-ESM-1-2-HAM	Max Planck Institute for Meteorology, Germany	1.875° × 1.875°
MPI-ESM1-2-HR	Max Planck Institute for Meteorology, Germany	0.9° × 0.9°
MPI-ESM1-2-LR	Max Planck Institute for Meteorology, Germany	1.875° × 1.875°
MRI-ESM2-0	Meteorological Research Institute, Japan	1.125° × 1.125°
NESM3	Nanjing University of Information Science and Technology, China	1.875° × 1.875°
NorESM2-LM	Norwegian Climate Centre, Norway	2.5° × 1.875°
NorESM2-MM	Norwegian Climate Centre, Norway	1.25° × 0.9375°
SAM0-UNICON	Seoul National University, Korea	0.95° × 1.25°
TaiESM1	Research Center for Environmental Changes, Academia Sinica, Chinese Taibei	0.9° × 1.25°
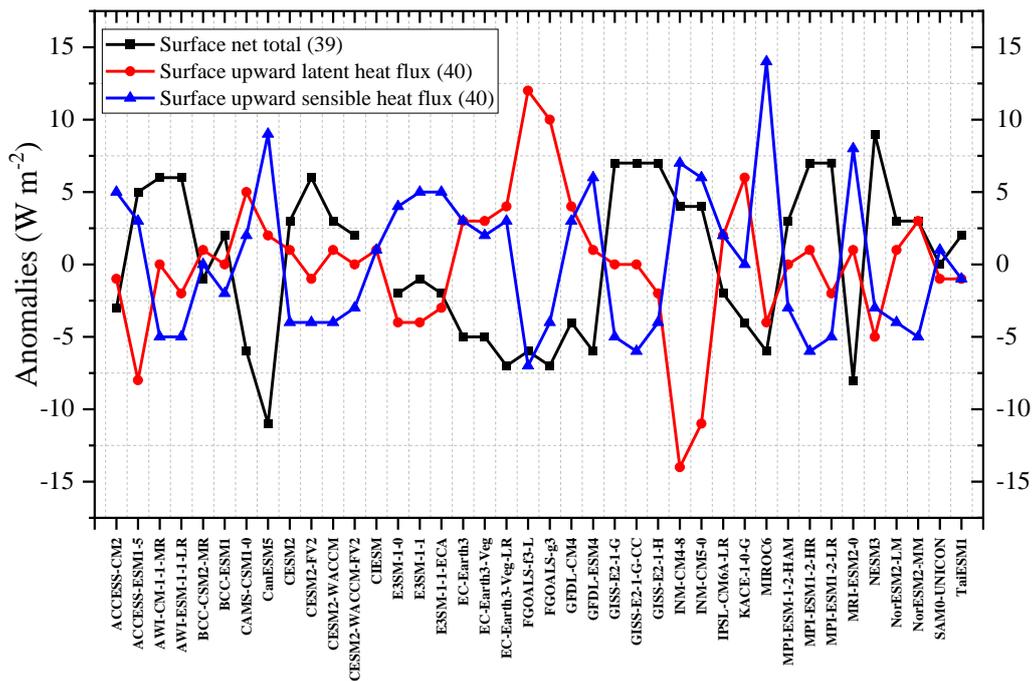
Figure S2. Annual land mean anomalies of surface net radiation (black line), latent heat fluxes (LH, red line), and sensible heat fluxes (SH, blue line) (Units: W m^{-2}) with regard to their respective multi-model means over East Asia as simulated by various CMIP6 models, respectively. The numbers in the parentheses indicate the available CMIP6 climate models for the corresponding radiation components.
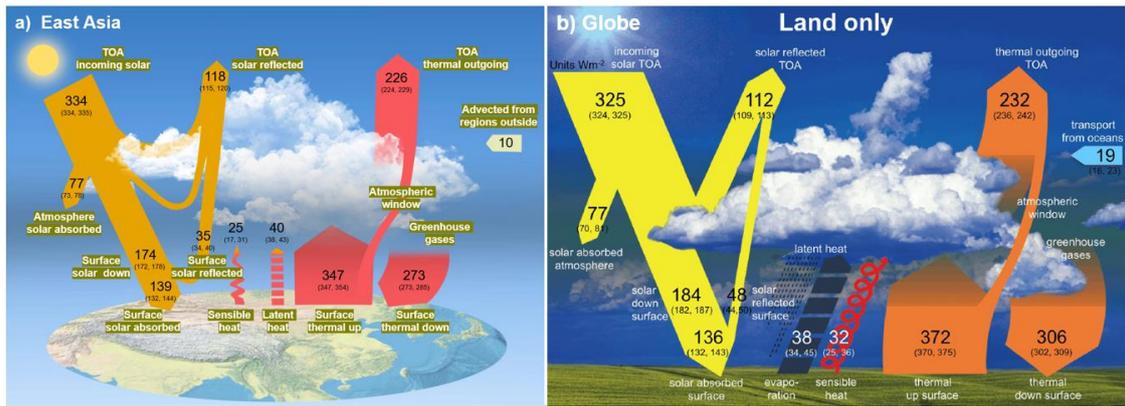
Figure S3. Comparisons of the present-day land mean energy balance diagrams over (a) East Asia (this study) and (b) globe (Wild et al. 2015), respectively, under all-sky conditions.
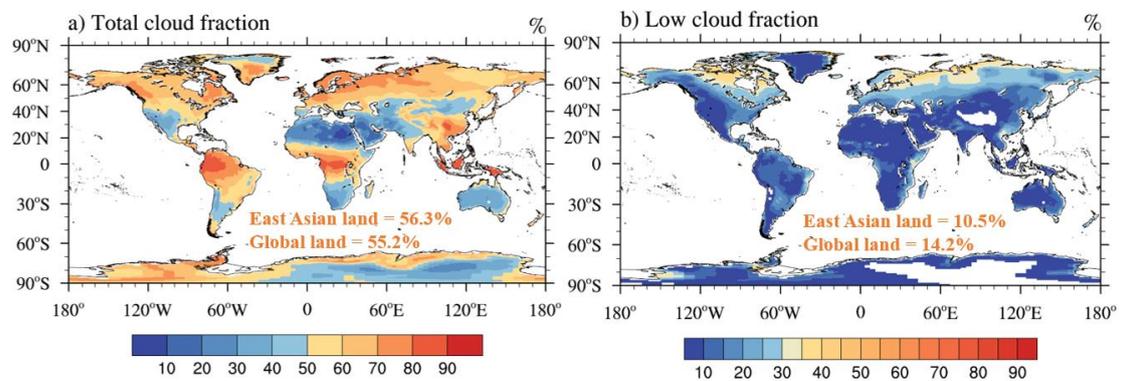
Figure S4. Distribution of global land mean (a) total and (b) low cloud fraction (CF) (Units: %) during 2010-2014. The clouds are derived from CERES_SSF1deg Ed4.1 product, which show similar distribution pattern with that retrieved from MODIS documented by Fan et al. (2018). Moreover, the area-weighted averages of them over East Asian land and global land are 56.3% and 55.2%, as well as 10.5% and 14.2%, respectively, suggesting a slightly more total CF of 1.1% and fewer low CF of 3.7% over East Asian land compared to the global land.
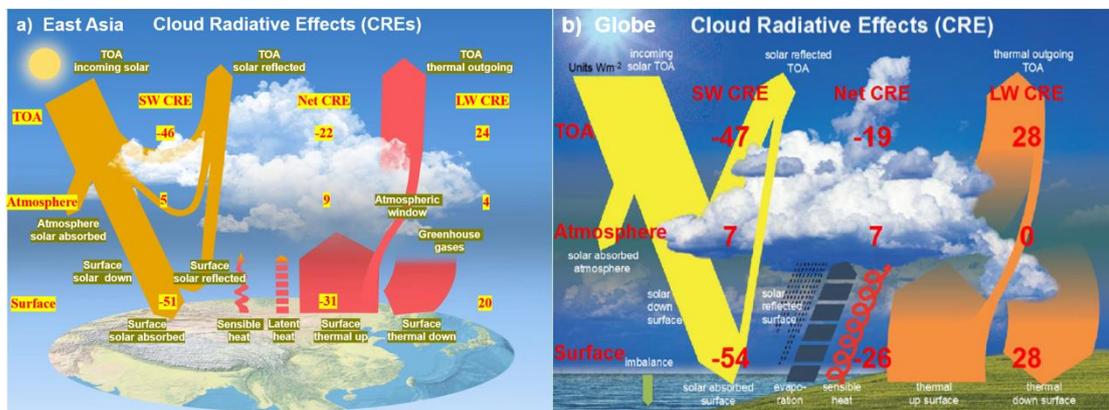
Figure S5. Comparisons of the present-day diagrams of the annual mean shortwave, longwave, and net (shortwave + longwave) cloud radiative effects (CREs) (Units: W m^{-2}) at the TOA, within the

atmosphere, and at the surface over (a) East Asian land (this study) and (b) globe (Wild et al. 2019).

Detailed analyses on clear-sky energy budgets are given as follows.

a. Shortwave components

The annual East Asian land-mean anomalies of SW absorption at the TOA, within the atmosphere, and at the surface with regard to their respective multi-model means under clear-sky conditions as simulated by various CMIP6 models are displayed in Fig. 1b. More detailed summaries of the CMIP6 models with respect to its clear-sky budget, the multi-model mean, the corresponding estimates from the CERES and ERA5 are given in Table 1. Large variations appear among different models in terms of their clear-sky annual land-mean SW absorption at the TOA and surface over East Asia, with a range of 24 and 36 W m^{-2} as well as a standard deviation of 6.9 and 7.8 W m^{-2}, respectively (Fig. 1b; Table 1), both showing larger uncertainties than that under all-sky conditions (Fig. 1a; Table 1). The estimated multi-model mean TOA absorbed clear-sky SW radiation is 258 W m^{-2}, differing by negative and positive deviations of 4 and 2 W m^{-2} from the CERES- and ERA5-derived estimates of 262 and 256 W m^{-2} (Table 1), respectively. The multi-model mean surface absorbed clear-sky SW radiation is estimated to be 189 W m^{-2}, which is within 2 W m^{-2} of the CERES-based estimate but differs as much as 10 W m^{-2} from the ERA5 estimate (Table 1). Specifically, for the SW clear-sky absorption at the surface simulated by various models, although their absolute values are around 27% ($\frac{257.5-189.1}{257.5} \times 100\%$) lower than at the TOA, they show a larger model spread and standard deviation between models (Table 1). Interestingly, despite the absolute values of the simulated SW absorption within the atmosphere under clear-sky conditions are slightly lower than that under all-sky conditions (69 vs. 73 W m^{-2}), they have the same model spread and standard deviation (19 and 3.8 W m^{-2}) (Table 1).

b. Best estimates for the surface downward SW radiation

Contrary to the all-sky conditions (Fig. 1a), the discrepancies of the simulated clear-sky surface downward SW radiation among different models are notably smaller than the surface absorbed SW radiation (Fig. 2a), with their respective clear-sky spreads of 25 and 36 W m^{-2} and standard deviations of 4.6 and 7.8 W m^{-2} (Table 1). Although the absolute values of the clear-sky SW downward radiation are larger than that under all-sky conditions, the relative discrepancy among different models with respect to the multi-model mean is much smaller, at around 10% ($\frac{25}{242} \times 100\%$) and 18% ($\frac{33}{186} \times 100\%$), respectively (Table 1).

In order to obtain more accurate SW downward radiation at the surface, we make use of the surface observations to reduce the uncertainties induced by various models. The clear-sky surface observational sites in China are taken from the homogenized monthly SSR data from the CMA (Yang et al. 2018, 2019), while we utilize the clear-sky CERES-interpolated estimates at the corresponding GEBA sites for the remaining East Asian sites as introduced above in Section 2.1.

Fig. 3b shows the distributions of the annual mean surface SW clear-sky radiation at 92 stations and the collocated rural and urban stations over East Asia. The high values of the clear-sky surface downward SW radiation are mainly located in the TP, with the highest value larger than 282 W m^{-2} (Naqu, Tibet) and an abnormal high value of 279 W m^{-2} located in Changning, Hunan (located at the southern China). For the convenience of comparison with the surface observations, the grid values from the multi-model mean, CERES, and ERA5 are then interpolated to the corresponding surface sites. The distributions of the annual mean biases of clear-sky surface downward SW radiation from different data sources (e.g., the CERES, multi-model mean, and ERA5) against surface observations (Figs. 7a, c, and e) as well as the corresponding comparisons of their respective annual land means at the surface sites with their observed counterparts are given in Figs. 7 b, d, and f. The CERES-derived clear-sky surface SW radiation is mainly overestimated in central and western China, with the maximum value reaching 40 W m^{-2}, which is distributed in the eastern TP and Xinjiang province (located at the northwestern China), while the slight underestimations are mainly located in northeastern, Eastern, and Southern China, within a range of 10 W m^{-2} (Fig. 7a). Both the distribution patterns and magnitudes of the clear-sky SSR biases from the CMIP6 multi-model mean and ERA5 estimates against the ground-based observations are consistent with each other, except for some individual sites over northeastern Inner Mongolia, eastern China, western Mongolia, and Japan (Figs. 7c and e). The clear-sky annual East Asian land means of surface solar radiation derived from CERES, CMIP6 multi-model mean, and ERA5 agree reasonably well with the surface observations, but with smaller correlation coefficients ranging from 0.78 to 0.82 compared to the all-sky conditions (Figs. 7b, d, and f). Based on the corresponding station mean biases at the surface observational sites listed in Table 2, the annual land mean surface solar radiation is significantly overestimated in the CMIP6 multi-model mean and ERA5 by 9.07 and 5.72 W m^{-2}, respectively, while much smaller overestimation appears in CERES with station mean bias of 0.35 W m^{-2}. The even distributed surface sites of overestimations and underestimations contribute to the small station mean bias in CERES-derived surface solar radiation (Fig. 7b), while more underestimations in rural stations (Fig. 7b) result in the negative rural station mean bias (Table 2). However, the urban and rural stations in ERA5, especially in CMIP6 multi-model mean, show high overestimations at surface sites, among which the urban stations are generally more overestimated than the rural stations (Figs. 7d and f; Table 2). On average, the annual East Asian land-mean area-weighted averages of clear-sky surface downward SW radiation from CERES, CMIP6 multi-model mean, and ERA5 all overestimate the surface observed counterpart of 230 W m^{-2}, with much higher biases of around 6, 12, and 8 W m^{-2}, respectively (Table 3). More negative biases over northeastern Inner Mongolia in ERA5 (Figs. 7c and e) are the reason for a closer area-weighted average surface SW clear-sky downward radiation with respect to the surface observations (Table 3) compared to that in CMIP6 multi-model mean.

Similar to the all-sky conditions, the best estimate for the surface downward SW clear-sky radiation is calculated based on the linear regression analysis on the model biases of various models

at 92 sites against their regional land means over East Asia, following again the methodology introduced in Wild et al. (2015). As shown in Fig. 6b, the correlation coefficient between them is 0.94, a little lower than the all-sky counterpart, suggesting that the higher clear-sky East Asian land mean value of a climate model comes with a stronger overestimation against ground-based observations. Thus, a best estimate for the clear-sky SSR is determined through the intersection between the linear regression line and zero bias line derived from the model biases with respect to the surface observations, that is 234±1.1 W m^{-2} (2σ uncertainty). This best estimate is around 2 and 4 W m^{-2} lower than the respective estimates from the CERES and ERA5 (Fig. 6b), which is similar to those under all-sky conditions (Fig. 6a). Likewise, most of the climate models (33/35) tend to overestimate the observed clear-sky downward solar radiation at the surface, with a multi-model mean overestimation of 9.1 W m^{-2}.

c.   Longwave components

The simulated annual East Asian land-mean anomalies of clear-sky net LW radiation at the TOA, within the atmosphere, and at the surface with respect to their respective multi-model means by various CMIP6 models are shown in Fig. 1d, along with more detailed model information and CERES- and ERA5-derived estimates (Table 1). From the TOA to surface, the simulated net LW radiation varies in a range of 15, 16, and 18 W m^{-2}, with a standard deviation of 3.2, 3.6, and 4.1 W m^{-2}, respectively, indicating that the discrepancies become larger between models as well as their relative discrepancies (6.1%, 11%, and 19%), which is similar to that under all-sky conditions but with smaller standard deviations (Table 1). Ultimately, the simulated East Asian multi-model mean net clear-sky LW radiation at the TOA, within the atmosphere, and at the surface is estimated to be -247, -151, and -95 W m^{-2}, respectively, which are very close to the estimates from the CERES and ERA5, with respective discrepancies within 3 and 1 W m^{-2} (Table 1). However, as can be seen from Fig. 2b and Table 1, the estimated East Asian annual land-mean surface downward and upward LW fluxes under clear-sky conditions differ greatly between models, with large standard deviations of 6.8 and 7.1 W m^{-2} and multi-model means of 256 and -351 W m^{-2}, respectively. Their deviations from the corresponding estimates from the CERES and ERA5 are no more than 2 and 4 W m^{-2}, respectively, which is significantly smaller than those under all-sky conditions (Table 1).

d.   Discussion of land energy balance over East Asia under clear-sky conditions

According to the above-mentioned estimates of the energy balance components under clear-sky conditions, a similar diagram of the present-day annual land-mean energy balance over East Asia is given in the Fig. 6b. It's noteworthy that the estimated magnitudes of clear-sky radiative components in this figure only represent the removal of cloud while the other atmospheric conditions remain the same as under all-sky conditions, which allows to study cloud effects. The TOA energy budgets under clear-sky conditions are also given by the most advanced CERES-derived product, with the estimated annual land-mean reflected solar radiation and OLR at the TOA of -72 and -250 W m^{-2}, respectively. The uncertainty ranges of clear-sky SW and LW TOA fluxes

(Fig. 6b) are according to Loeb et al. (2018), which documented the regional uncertainties of 5.4 and 4.6 W m^{-2}, respectively, twice of those for all-sky conditions.

As discussed in section 4.2, the best estimate for the clear-sky annual land-mean SSR is 234 W m^{-2}, the lower value of uncertainty range is given by the lowest individual model estimate, while the higher value is from the CERES-derived estimate, that is 228–236 W m^{-2} (Fig. 6b). Similar to the all-sky conditions, the calculated clear-sky radiation weighted surface albedo is near 0.19 (44.8/235.6), the resulting surface reflected and absorbed SW fluxes are -44 and 190 W m^{-2}, respectively. Additionally, the corresponding estimates of surface albedos from the multi-model mean and ERA5 are 0.218 (52.7/241.8) and 0.247 (58.9/238.2), respectively, which largely differ from the CERES-derived estimate, particularly for the estimate from ERA5 reanalysis, showing a similar tendency with that under all-sky conditions. Again, the uncertainty range of the estimated reflected surface solar radiation is given by the various models, multi-model mean, and CERES-based estimate, ranging from 40 to 53 W m^{-2}, while the counterparts of the absorbed SW radiation are based on the multi-model mean, CERES, and ERA5 estimates, in a range of 175 and 196 W m^{-2}. Consequently, the atmospheric SW absorption is estimated to be 72 W m^{-2}, with its uncertainty range of 69–77 W m^{-2} determined by the different individual estimates outlined above.

According to the ERA5 reanalysis, the clear-sky annual East Asian land-mean surface upward and downward LW radiation are estimated to be -347 and 253 W m^{-2}, with uncertainty ranges of 253–256 and 347–353 W m^{-2}, respectively, referring to the estimates from different data sources. The clear-sky net LW fluxes at the surface and within the atmosphere are then calculated to be -94 and -156 W m^{-2}, respectively.

In summary, for clear-sky conditions over East Asian land, about 21.6% of the TOA incoming solar radiation is absorbed by the atmosphere, while around 56.9% is absorbed at the Earth's surface. However, the all-sky atmospheric and surface solar absorption account for 23.1% and 41.6% of the TOA incident solar radiation, respectively, implying that the existence of clouds results in more SW absorption within the atmosphere of around 1.5% and much less solar absorption of around 15.3% at the surface with respect to the TOA incoming solar radiation.